Optical Engineering

OpticalEngineering.SPIEDigitalLibrary.org

Interaction properties between different modes of localized and propagating surface plasmons in a dimer nanoparticle array

Qilin Ma
Guangqiang Liu
Sujuan Feng
Yiqing Chen
Weiping Cai

SPIE.

Qilin Ma, Guangqiang Liu, Sujuan Feng, Yiqing Chen, Weiping Cai, "Interaction properties between different modes of localized and propagating surface plasmons in a dimer nanoparticle array," *Opt. Eng.* **57**(8), 087108 (2018), doi: 10.1117/1.OE.57.8.087108.

Interaction properties between different modes of localized and propagating surface plasmons in a dimer nanoparticle array

Qilin Ma,[a,b] Guangqiang Liu,[b,*] Sujuan Feng,[c,*] Yiqing Chen,[a] and Weiping Cai[b]
[a]Hefei University of Technology, School of Materials Science and Engineering, Hefei, Anhui, China
[b]Chinese Academy of Sciences, Institute of Solid State Physics, Key Laboratory of Materials Physics, Anhui Key Laboratory of Nanomaterials and Nanotechnology, Hefei, China
[c]Qufu Normal University, School of Physics and Engineering, Shandong Provincial Key Laboratory of Laser Polarization and Information Technology, Qufu, China

Abstract. When the peak positions of propagating surface plasmon polaritons (SPPs) and localized surface plasmon resonances (LSPRs) become very close to each other in a single nanoparticle array structure, an anticrossing behavior of the surface plasmon resonances (SPRs) peak positions usually occurs, which can considerably enhance the near-field intensity. We first report on the interaction of two types of SPRs in a dimer nanodisk–SiO_2 spacer–gold film hybrid sandwich structure. The anticrossing behavior does not appear always due to various modes of LSPRs in such structures. Moreover, a crossing behavior also appears based on the interaction of SPPs and a longitudinal bonding mode of LSPRs. When the anticrossing behavior occurs, a bandgap that changes only with the array period also appears. This bandgap influences the electric field intensity enhancement not only in the anticrossing behavior but also in the crossing behavior. The electric field intensity distribution properties both in the anticrossing behavior and crossing behavior are discussed with reference to the hybrid properties of the SPPs and LSPRs modes. Furthermore, we report on the occurrence mechanisms of these different behaviors. [DOI: 10.1117/1.OE.57.8.087108]

Keywords: plasmon interaction; surface plasmon polaritons; localized surface plasmon resonances; electric field intensity enhancement.

Paper 180608 received May 4, 2018; accepted for publication Aug. 15, 2018; published online Aug. 29, 2018.

1 Introduction

Surface plasmon resonances (SPRs) can be classified into two types:[1] surface plasmon polaritons (SPPs), a kind of evanescent wave that propagates along the interface between a metal and dielectric, and localized surface plasmon resonances (LSPRs), a nonpropagating mode located at the surface of a nanoparticle. Due to the fact that SPPs can be excited and propagated in nanostructures, various devices toward wide fields based on SPPs have been designed and studied, such as optical waveguides,[2,3] optical super lenses,[4] plasmonic filters,[5] sensing,[6] etc. As in nonpropagating SPRs, LSPRs are located on the surface of nanoparticles and induce ultrahigh localized electric field intensities, especially in the gap regions of dimer nanostructures.[7–10] Therefore, LSPRs are widely applied in surface-enhanced Raman scattering (SERS),[11–14] surface-enhanced fluorescence,[15] etc. Schmidt et al.[16] reported different modes in single nanoparticles, such as dipole, quadrupole, hexapole, etc. Moreover, for the dimer structure, different kinds of LSPR modes can be observed.[17,18] Predictably, the interaction between SPPs and LSPRs may result in some extraordinary optical properties for realizing innovative applications. Generally, coupling these two types of SPRs significantly enhances the localized electric field intensity. An anticrossing behavior of LSPR and SPP peak positions can usually be observed when the two types of SPR peaks approach each other. Cesario et al.[19] first reported that the LSPR and SPP coupled hybrid mode comprises two peaks in a sandwich structure with nanodisk array. The anticrossing properties were investigated by Chu and Crozier[20] in a similar structure, and their further studies[21] revealed the relevance of coupling characteristics to electric field intensity enhancement at the anticrossing positions. Zhou et al.[22] simulated the electric field intensity enhancement in a bowtie and nanodisk hybrid array with coupling of LSPRs and SPPs, and obtained a value about an order of magnitude higher than that obtained for a plain bowtie array. However, in general, the interaction mechanism between LSPRs and SPPs is still unclear. Furthermore, most studies focus on single nanoparticle arrays, and the optical properties of the coupling between SPPs and LSPRs in a dimer nanoparticle array structure have not yet been systematically studied.

In this work, we studied the coupling between SPPs and LSPRs with different modes in dimer nanodisk array–SiO_2–Au sandwich structures. We also observed and reported the mechanisms of both anticrossing and crossing behaviors. In addition to the classical anticrossing phenomenon, a crossing behavior has been observed, where the electric field intensity achieves a minimum value at the crossing position, which can be attributed to the mismatch of energy gathering positions of SPPs and LSPRs. Furthermore, we monitored the electric field intensities and distribution properties in different conditions (with varying array period and thickness of nanodisks) and analyzed the electric field properties using the widely used and reliable finite-difference time-domain method.

*Address all correspondence to: Guangqiang Liu, E-mail: liugq@issp.ac.cn; Sujuan Feng, E-mail: sjfeng@aiofm.ac.cn

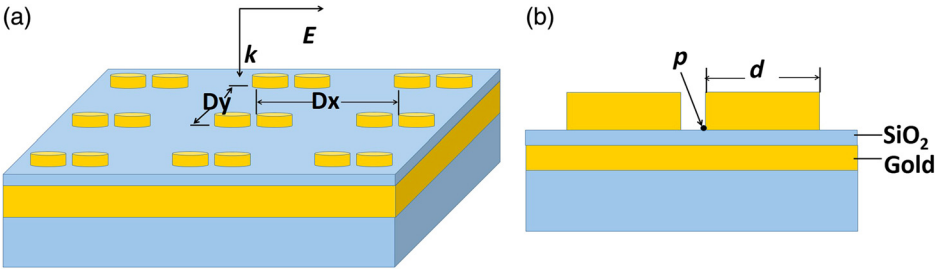

Fig. 1 Schematic of the sandwich structure: (a) three-dimensional view and (b) cross-sectional view.

2 Structure Design

The schematic diagram of the dimer nanodisk array–SiO_2–Au sandwich structure is shown in Fig. 1. The sandwich structure is constructed using Au and SiO_2 films with fixed thickness besides dimer nanodisks array with tunable thickness. The Au film is 150-nm thick, which is sufficient to avoid direct light transmission, and the thickness of the SiO_2 spacer is 30 nm. The diameter (d) of nanodisks is fixed at 100 nm and the gaps in dimer nanodisks are kept at 10 nm. The long disk pair axis is parallel to the x-axis. The array periods at the x-axis (D_x) and the y-axis (D_y) are both set at 720 nm ($D_x = D_y = 720$ nm) initially. The incident light is chosen to be a plane wave with linear polarization direction parallel to the x-axis and incident direction perpendicular to the disk array. In our simulations, we have adopted a SiO_2 refractive index of 1.46 and a wavelength-dependent refractive index of Au from Johnson and Christy's work.[23]

3 Results and Discussion

Figure 2 shows the charge distribution of the longitudinal bonding mode and longitudinal antibonding mode obtained in the simulation. Four LSPR modes have been observed earlier using electron energy loss spectrum in different kinds of dimer nanoparticles,[17,18,24] and the charge distribution characteristics of the modes have been described by simulation. These modes are based on dipole–dipole interactions, compared to the dipole LSPR mode in a single nanoparticle. Considering the distribution of positive and negative charges,[7] these modes are classified into longitudinal or transverse modes. However, in our simulations, only two longitudinal modes [Figs. 2(a) and 2(b)] and no transverse modes have been observed. In the simulations, a polarized incident light was used as an excitation source. When the longitudinal direction is parallel to the electric field polarization direction of the incident light, only two LSPR modes could appear in the stimulation results, namely, the longitudinal bonding mode (dipolar bright mode) and longitudinal antibonding mode (dipolar dark mode).[24] The transverse modes were hidden because of the electric field polarization property of the exciting light.

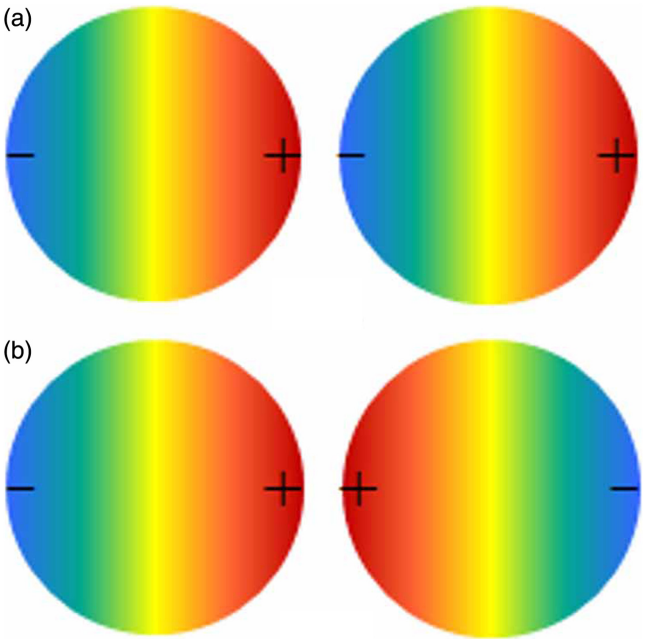

Fig. 2 Eigencharge distributions of the dimer nanodisks in the simulation: (a) longitudinal bonding mode and (b) longitudinal antibonding mode.

In dimer nanodisks, for two mutually interacting dipoles with a consistent dipole electric field direction, the longitudinal bonding mode usually has the longer resonance peak wavelength. However, the longitudinal antibonding mode is usually located in the ultraviolet (UV) region and, therefore, needs to be redshifted, which we monitored in this study. For a 40-nm thickness, only one LSPR mode (longitudinal bonding mode) resonance position was observed in our monitored region. The corresponding LSPR absorption peak position was found to be at 756 nm. Owing to similar oscillation characteristics, the longitudinal bonding mode could be equivalent to the dipolar mode, which means that the dimer nanoparticles could be equivalent to a single one. It can be predicted that the anticrossing behavior can also appear when this mode and SPPs approach each other. However, the different dipole electric field directions in antibonding modes may lead to a very different result. To verify these predictions, the near-field spectral characteristic was stimulated with tuned array period and nanodisk thickness.

Generally, SPPs cannot couple with light directly at the plane metal surface due to their larger momentum compared to the optical wave momentum at the same frequency. Thus, some special structures that can provide additional momentum are necessary. To date, several techniques have been used to excite SPPs, such as prism coupling excitation,[25] grating coupling excitation,[26] nanostructure scattering excitation,[27] etc. In the case of nanoparticle array, there is an additional momentum, $G = (2\pi/D)(p_2 + q_2)^{1/2}$, where D is the grating constant, and p and q are the integers.[19] The SPPs can be excited when G couples incident light into SPPs on the Au film. For the array structure with $D_x = 720$ nm, the SPP mode of $(p, q) = (1,0)$ is located

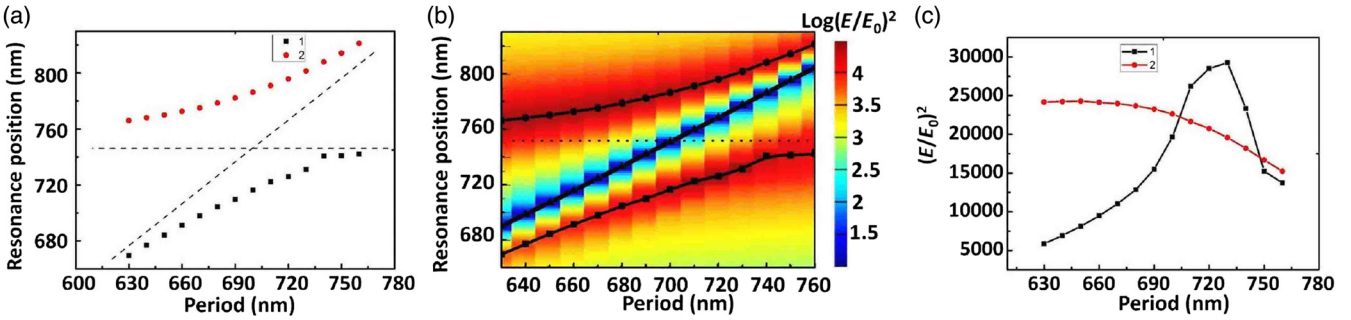

Fig. 3 For a thickness of 40 nm, (a) the resonance positions with different periods, (b) color map of the electric field intensity enhancement with different periods and the ravine curve, and (c) the corresponding electric field intensity enhancement at point *p*.

at 723 nm, which is the closest one to 756 nm. The electric field intensity property at p [shown in Fig. 1(b)], where the gap region of the particle edge is located, was monitored due to the fact that the strongest electric field intensity enhancement for dimer structure usually occurs at such a position. The period of D_x was tuned from 630 to 760 nm with a 10-nm gradient. The corresponding resonance peak positions at different D_x values are shown in Fig. 3(a), where two resonance peaks are observed and redshifted as D_x increases. When the period of D_x was tuned from 630 to 760 nm, the mode of resonance peak 1 [as is shown in Fig. 3(a) legend 1] changes from LSP to SPP; on the contrary, the mode of resonance peak 2 [as is shown in Fig. 3(a) legend 2] changes from LSP to SPP mode. So that an anticrossing behavior is clearly observed.

To explain the reasons for the emergence of the anticrossing behavior, the local electric field intensity enhancement factor $[(E/E_0)^2]$ versus the period is discussed in detail. The local electric field intensity $(E/E_0)^2$ at point p is monitored to elucidate the local electric field intensity $(E/E_0)^2$ characteristics at the resonance peaks. The color map of the logarithm of the electric field intensity, log $(E/E_0)^2$, at point p and the resonance peak positions are shown in Fig. 3(b). The ravine region curve linearly changes with the period and is free from the influence of LSPR and SPP positions appearing in the color map, as shown in Fig. 2(b).

The ravine region is like a bandgap, which results in the anticrossing behaviors. Further study indicates that this bandgap, usually near the SPPs, influences the SPPs peak width and changes with change in period (not shown in this report). The period-dependent bandgap, which cannot focus much energy, is called SPPs-induced bandgap (SPPs-IBG). Even though the SPPs-IBG prevents the strong coupling of the SPP and LSPR, which results in an anticrossing behavior, the electric field intensity enhancement is improved at both positions of the resonance peaks, compared to the simple LSPR mode. The maximum electric field intensity enhancement is 2.95×10^4 obtained at the period of 730 nm, as shown in Fig. 3(c). This value is about twice that for LSPR without the anticrossing influence. And also, it can be seen from Fig. 3(a) that when changing the period, the SPR peak position changes. This means that the SPR position is tunable in a wide range. Therefore, it can be adjusted and controlled to obtain the optimized SERS signal when we use a different wavelength of light source to detect a different molecule. For example, when the period is 700 nm, one of the SPR positions is at 787 nm, which is very close to 785 nm (a common wavelength for the near-infrared SRES detection).

To investigate the near-field electric field distributions of SPPs-IBG and the resonance peak positions, the distributions corresponding to the period of 700 nm at 716, 787, and 751 nm were monitored and are shown in Figs. 4(a)–4(c), respectively. Among these, 716 and 787 nm are the resonance peak positions, and 751 nm is in the SPPs-IBG region. Both LSPR and SPP electric field intensity

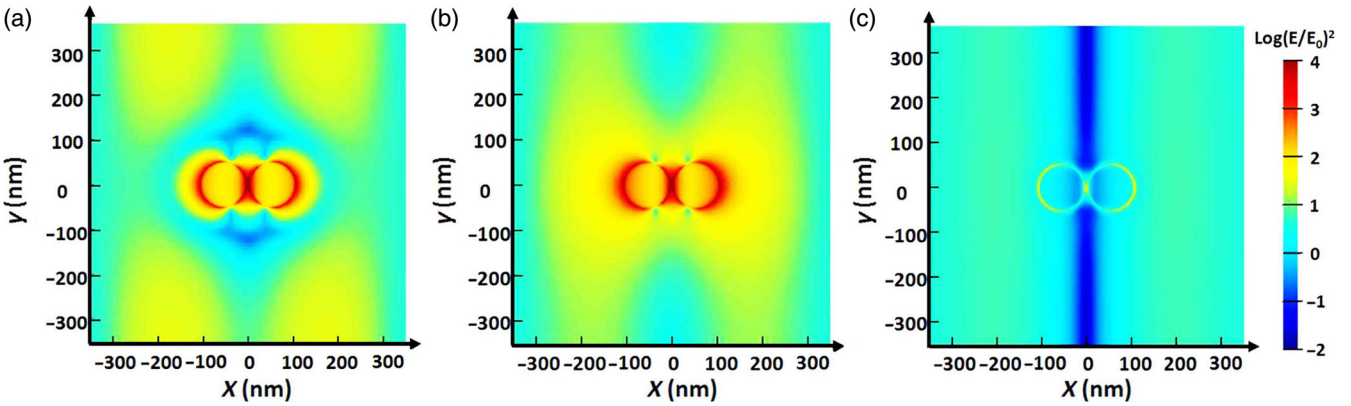

Fig. 4 Electric field intensity distribution $[\log (E/E_0)^2]$ at the incident light wavelength of (a) 716, (b) 787, and (c) 751 nm.

distribution properties are presented at 716 and 787 nm, respectively, which means that the two resonance peaks represent LSPR and SPP hybrid modes. Although the electric field intensity distribution property of SPPs-IBG at 751 nm is largely similar to that of the SPPs mode, not much energy can be collected to form an absorption peak, and LSPRs excitation and enhancement are also restricted.

The coupling properties between longitudinal antibonding mode and SPPs were also studied. Because the resonance peak of longitudinal antibonding mode is not in our wavelength monitor range, but in the UV region, it needs to be redshifted. With the two modes in the nanodisk dimer (shown in Fig. 2), synergistic oscillations between the top and bottom of the nanodisks are exhibited, thus indicating that the thickness of the nanodisks can influence the LSPRs peak positions. To redshift the longitudinal antibonding mode to a position near the SPP mode, the thickness of the nanodisks was increased. The period of the dimer nanodisks was fixed at 720 nm, and other parameters were not changed, except for the nanodisks thickness. The corresponding SPP absorption peak position was at 723 nm. The LSPR of longitudinal antibonding mode redshifted as the nanodisk thickness increased from 90 to 170 nm. The thickness was independent of the SPP absorption peak position at 723 nm. Figure 5(a) shows the LSPR of longitudinal antibonding mode and SPP peak positions with different thicknesses of nanodisks. In Fig. 5(a), no anticrossing behavior but a crossing behavior is observed. This is obviously different from the anticrossing behavior in previous reports.[19–21] This difference is ascribed to the difference of electric field oscillation characteristics between antibonding and bonding modes. Even though the gap is very small (10 nm), strong coupling would appear both in the bonding and antibonding modes. However, these two modes also show some difference in the gap region. The oscillation energy is higher at the outer nanodisk edges than that at the gap region for the longitudinal bonding mode, and vice versa for the longitudinal antibonding mode.[24] The electric field intensity $(E/E_0)^2$ enhancement at point p was monitored and is shown in Fig. 5(b). The $(E/E_0)^2$ value improved with the increase of the nanodisk thickness. However, an apparent trough at the thickness of 140 nm was observed. This resulted from the combined effects of LSPRs and SPPs.

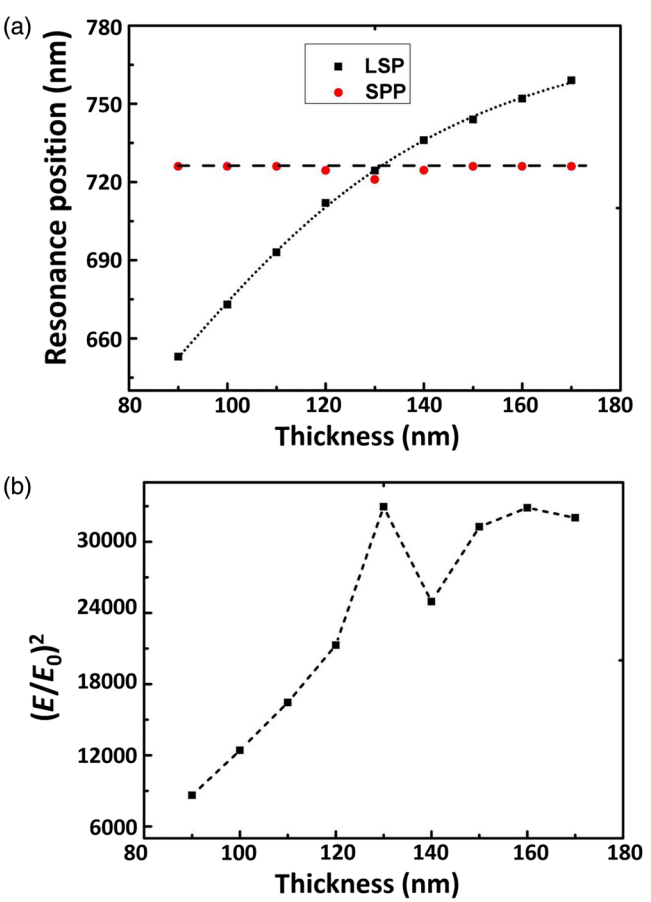

Fig. 5 (a) Resonance positions with different nanodisk thickness and (b) the corresponding electric field intensity enhancement at point p.

The influences of the period were also studied by fixing the nanodisk thickness at 130 nm and tuning the period from 630 to 760 nm. The peak position changing curves are shown in Fig. 6(a), and a similar crossing behavior appears. The corresponding $(E/E_0)^2$ versus period plot is shown in Fig. 6(b). The $(E/E_0)^2$ value is improved with the period increasing below 680 nm and decreasing over 740 nm. A trough appears between 680 and 740 nm near the crossing position, and the minimum value was achieved at about 710 nm, which is about 70% of that obtained from the 680-nm period. Figure 6(c) shows the color map of the logarithm of electric field intensity enhancement with different periods at point p. The SPPs-IBG is represented by the dotted line shown in Fig. 6(c) and resulted in a decrease in electric field intensity enhancement $(E/E_0)^2$ at point p. However, it did not result in an anticrossing behavior in this case.

Under the longitudinal antibonding mode, usually a strong electromagnetic oscillation can be observed in the gap region, which prevents SPPs-IBG from influencing the peak position and further results in the disappearance of the anticrossing behavior. Generally, crossing behavior indicates strong coupling and can provide higher $(E/E_0)^2$. However, in this case, the crossing behavior corresponds to smaller $(E/E_0)^2$. In general, an enhancement of electric field intensity means that energy is focused together. However, in our case, conversely, it means a smaller $(E/E_0)^2$. The distribution of electric field intensity of the SPP modes is monitored, and Fig. 6(d) shows the distribution of electric field intensity of the SPP at the period of 760 nm as an example. The dotted line in Fig. 6(d) shows the strongest electric field amplitude intensity position, it means that the strongest electric field energy region of the SPPs mode is not located at the nanoparticle but at a position about one fourth of D_x between the center of the dimer nanoparticles, which is similar to the work that Ghoshal and Kik[28] showed. Also, because of the mismatch of the phase between SPP and LSP [Fig. 6(d) shows], the energy focused region of SPPs and longitudinal antibonding mode is mismatched, which decreases energy focusing in the gap region and, eventually, leads to a smaller electric field intensity enhancement. Additionally, the SPPs-IBG hinders the focusing of energy stated above; this also contributes to a lower enhancement in the gap region.

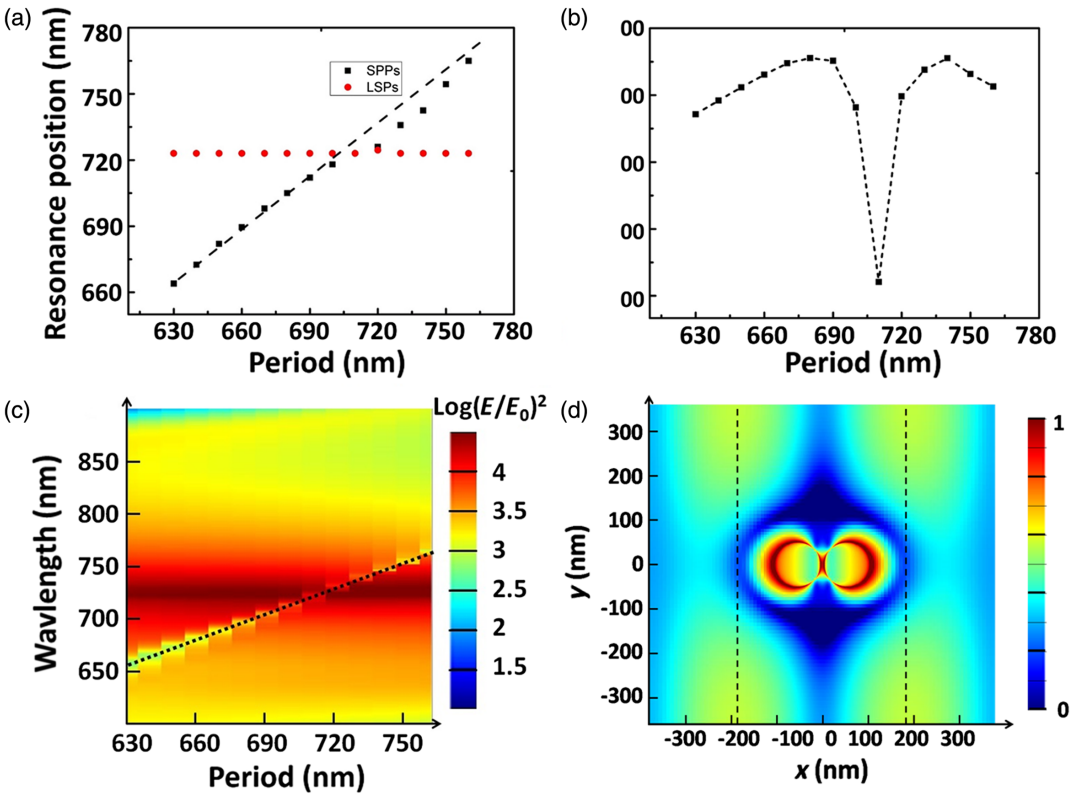

Fig. 6 (a) Resonance positions with different periods, (b) the corresponding electric field intensity enhancement of LSPR, (c) the color map of the logarithm of electric field intensity enhancement with different periods at point *p*, and (d) the normalized electric field intensity distribution of SPP mode at the period of 760 nm, the excitation wavelength is 765 nm.

4 Conclusions

This report discussed the interaction of LSPRs and SPPs in a dimer nanodisk–SiO_2 spacer–gold film hybrid sandwich structure. Both an anticrossing behavior and a crossing behavior of the LSPR and SPP resonance positions were observed. Further investigation demonstrated that the emergence of crossing or anticrossing behavior depends on different LSPRs modes. The bonding mode can cause an anticrossing behavior, whereas the antibonding mode can induce a crossing behavior. An SPPs-IBG similar to the bandgap of SPRs that changed with period was observed. This resulted in the anticrossing behavior and decreased the $(E/E_0)^2$ value in the crossing region. Both the SPPs and longitudinal antibonding mode of the resonance peak positions were slightly blueshifted at the crossing location and a sharp decrease of the electric field intensity enhancement also appeared. Hence, this report presents a systematic study on the optical properties of dimer nanodisk–SiO_2 spacer–gold film hybrid sandwich structure. The results presented here can help to better understand the interaction characteristics between LSPRs and SPPs, which may play a guiding role in the study and design of plasmon devices, such as in SERS and biosensors.

Acknowledgments

This work was financially supported by the National Key Research and Development Program of China (Grant No, 2017YFA0207101) and the National Natural Science Foundation of China (Grant Nos. 51531006, 11604343, 11574313, and 51571188).

References

1. M. E. Stewart et al., "Nanostructured plasmonic sensors," *Chem. Rev.* **108**(2), 494–521 (2008).
2. J. Gosciniak et al., "Thermo-optic control of dielectric-loaded plasmonic waveguide components," *Opt. Express* **18**(2), 1207–1216 (2010).
3. Y. B. Wang et al., "Plasmon-induced transparency effect in metal-insulator-metal waveguide coupled with multiple dark and bright nanocavities," *Opt. Eng.* **55**(2), 027108 (2016).
4. E. T. Rogers et al., "A super-oscillatory lens optical microscope for subwavelength imaging," *Nat. Mater.* **11**(5), 432–435 (2012).
5. H. Lu et al., "Tunable band-pass plasmonic waveguide filters with nanodisk resonators," *Opt. Express* **18**(17), 17922–17927 (2010).
6. A. Li et al., "Ultrahigh enhancement of electromagnetic fields by exciting localized with extended surface plasmons," *J. Phys. Chem. C* **119**(33), 19382–19389 (2015).
7. W. Rechberger et al., "Optical properties of two interacting gold nanoparticles," *Opt. Commun.* **220**(1–3), 137–141 (2003).
8. P. H. Camargo et al., "Measuring the SERS enhancement factors of dimers with different structures constructed from silver nanocubes," *Chem. Phys. Lett.* **484**(4–6), 304–308 (2010).
9. S. Kim et al., "High-harmonic generation by resonant plasmon field enhancement," *Nature* **453**, 757–760 (2008).
10. Q. L. Ma et al., "Surface plasmon resonance and polarization change properties in centrosymmetric nanoright-triangle dimer arrays," *Opt. Eng.* **57**(3), 036112 (2018).
11. Y. C. Cao et al., "Nanoparticles with Raman spectroscopic fingerprints for DNA and RNA detection," *Science* **297**(5586), 1536–1540 (2002).
12. J. A. Dieringer et al., "A frequency domain existence proof of single-molecule surface-enhanced Raman spectroscopy," *J. Am. Chem. Soc.* **129**(51), 16249–16256 (2007).
13. S. M. Nie and S. R. Emery, "Probing single molecules and single nanoparticles by surface-enhanced Raman scattering," *Science* **275**(5303), 1102–1106 (1997).
14. H. Xu et al., "Spectroscopy of single hemoglobin molecules by surface enhanced Raman scattering," *Phys. Rev. Lett.* **83**(21), 4357–4360 (1999).

15. J. Zhang et al., "Surface-enhanced fluorescence of fluorescein-labeled oligonucleotides capped on silver nanoparticles," *J. Phys. Chem. B* **109**(16), 7643–7648 (2005).
16. F. P. Schmidt et al., "Morphing a plasmonic nanodisk into a nanotriangle," *Nano Lett.* **14**, 4810–4815 (2014).
17. G. Haberfehlner et al., "Correlated 3D nanoscale mapping and simulation of coupled plasmonic nanoparticles," *Nano Lett.* **15**, 7726–7730 (2015).
18. V. Flauraud et al., "In-plane plasmonic antenna arrays with surface nanogaps for giant fluorescence enhancement," *Nano Lett.* **17**, 1703–1710 (2017).
19. J. Cesario et al., "Electromagnetic coupling between a metal nanoparticles grating and a metallic surface," *Opt. Lett.* **30**, 3404–3406 (2005).
20. Y. Chu and K. B. Crozier, "Experimental study of the interaction between localized and propagating surface plasmons," *Opt. Lett.* **34**, 244–246 (2009).
21. Y. Chu et al., "Double resonance surface enhanced Raman scattering substrates: an intuitive coupled oscillator model," *Opt. Express* **19**(16), 14919–14928 (2011).
22. F. Zhou et al., "Huge local electric field enhancement in hybrid plasmonic arrays," *Opt. Lett.* **39**, 1302–1305 (2014).
23. P. B. Johnson and R. W. Christy, "Optical constants of the noble metals," *Phys. Rev. B* **11**, 1315–1323 (1975).
24. H. Duan et al., "Nanoplasmonics: classical down to the nanometer scale," *Nano Lett.* **12**, 1683–1689 (2012).
25. A. Otto, "Excitation of non-radiative surface plasma waves in silver by the method of frustrated total reflection," *Z. Phys.* **216**, 398–410 (1968).
26. Y. Teng and E. A. Stern, "Plasma radiation from metal grating surfaces," *Phys. Rev. Lett.* **19**, 511–514 (1967).
27. H. Ditlbacher et al., "Fluorescence imaging of surface plasmon fields," *Appl. Phys. Lett.* **80**, 404–406 (2002).
28. A. Ghoshal and P. G. Kik, "Theory and simulation of surface plasmon excitation using resonant metal nanoparticle arrays," *J. Appl. Phys.* **103**(11), 113111 (2008).

Qilin Ma received his BS degree from Hefei University of Technology. Currently, he is a PhD candidate at Hefei University of Technology. He is working on investigating localized surface plasmon resonance and surface plasmon polariton interaction mechanisms and designing plasmon waveguide-based devices.

Guangqiang Liu is a researcher at the Institute of Solid Physics, Chinese Academy of Sciences. His main research interests include the design of noble metal micro/nanostructure arrays and control of its surface plasmon resonance, surface-enhanced Raman scattering detection, and developing sensors in the fields of food safety and environment.

Sujuan Feng is a researcher who received her PhD from Anhui Institute of Optics and Fine Mechanics, Chinese Academy Sciences. She worked at the Shandong Provincial Key Laboratory of Laser Polarization and Information Technology. Her main research interests are fiber lasers and amplifiers.

Yiqing Chen is a professor and doctoral tutor at Hefei University of Technology. His main research interests include synthesis, growth mechanisms, structural characterization and physical properties of quasi-one-dimensional nanomaterials, solar cell devices, and Hyundai motor new materials and their applications.

Weiping Cai is a researcher and doctoral tutor at the Institute of Solid State Physics, Hefei Institute of Material Science, Chinese Academy of Sciences. His main research interests include the construction of micro/nanostructure array and its devices, micro/nano hierarchical materials synthesis and its physical/chemical properties, and surface-enhanced Raman scattering detection and sensors in food safety and environment.